Check for updates

JGR Solid Earth

RESEARCH ARTICLE
10.1029/2025JB032670

Bayesian Inference of Local Paleosecular Variation From Sparse Paleomagnetic Data

M. A. Schanner[1], **R. Meyer**[2], **and L. V. de Groot**[2]

[1]GFZ Helmholtz Centre for Geosciences, Potsdam, Germany, [2]Palaeomagnetic Laboratory Fort Hoofddijk, Department of Earth Sciences, Utrecht University, Utrecht, The Netherlands

Key Points:

- A new method for paleosecular variation curve construction is presented
- Global magnetic field models can be used as a prior in regions of sparse data coverage
- Complex age distributions, due to archeological and radiocarbon dating, are reflected in the posterior ensemble

Correspondence to:
M. A. Schanner,
maximilian.schanner@gfz.de

Citation:
Schanner, M. A., Meyer, R., & de Groot, L. V. (2026). Bayesian Inference of local paleosecular variation from sparse paleomagnetic data. *Journal of Geophysical Research: Solid Earth*, *131*, e2025JB032670. https://doi.org/10.1029/2025JB032670

Received 14 AUG 2025
Accepted 6 FEB 2026

Author Contributions:
Conceptualization: M. A. Schanner, L. V. de Groot
Data curation: R. Meyer
Formal analysis: M. A. Schanner, R. Meyer, L. V. de Groot
Funding acquisition: L. V. de Groot
Investigation: M. A. Schanner
Methodology: M. A. Schanner, R. Meyer
Software: M. A. Schanner
Supervision: L. V. de Groot
Validation: M. A. Schanner, R. Meyer
Visualization: M. A. Schanner
Writing – original draft: M. A. Schanner
Writing – review & editing: R. Meyer, L. V. de Groot

© 2026. The Author(s).
This is an open access article under the terms of the Creative Commons Attribution License, which permits use, distribution and reproduction in any medium, provided the original work is properly cited.

Abstract We introduce a novel Bayesian method to construct local paleosecular variation (PSV) curves. By modeling the geomagnetic field as a Gaussian process, global models can be incorporated as informative prior distributions. Because we use Hamiltonian Monte-Carlo methods, complex age distributions resulting for example from radiocarbon calibration can be incorporated in the model. This improves PSV reconstruction in poorly sampled intervals and allows age refinement of individual records. We validate the method with synthetic data and apply it to the Azores, demonstrating its effectiveness in data-limited regions. The approach is implemented in an open-source Python package.

Plain Language Summary We present a new way to build local representations of how Earth's magnetic field has changed over time, even when only limited data are available. Our method uses global magnetic field models as a guide and can handle complex dating information, such as the uncertainties that come with radiocarbon dating. This helps create more accurate magnetic field curves and can improve the age estimates of individual samples. We tested the method on simulated data and real data from the Azores, showing that it works well in areas with few measurements. The method is freely available as a Python software package.

1. Introduction

Full vector paleosecular variation (PSV) curves describe local changes in the Earth's magnetic field. In contrast to global field models, which often smooth local rapid variations, PSV curves show the small scale behavior, such as geomagnetic jerks or spikes (Ertepinar et al., 2020; Yu et al., 2010) of the Earth's magnetic field at that specific location. Additionally, a high quality PSV curve may be used as an archeomagnetic dating tool (e.g., Béguin et al., 2021; Böhnel et al., 2016; McIntosh & Catanzariti, 2006; Pavón-Carrasco et al., 2011).

Creating a local PSV curve is relatively easy in areas where there is a large amount of paleomagnetic data available. Most recent studies constructing PSV curves (e.g., Mexico (Mahgoub et al., 2019), South America (Goguitchaichvili et al., 2019) and Iberia (Molina-Cardín et al., 2018)) are based on the bootstrap algorithm approach by Thébault and Gallet (2010), several other PSV curves are based on Bayesian methods (Hellio et al., 2014; Lanos, 2004; Lanos et al., 2005; Livermore et al., 2018). All of these approaches require a dense data input. However, a large paleomagnetic data set is not always available as the temporal and spatial distribution of paleomagnetic data are poor. For example, most paleomagnetic data come from the Northern Hemisphere, whereas data from the Southern Hemisphere, especially before 0 CE, remains scarce (Brown et al., 2021). Besides the spatially sparse distribution of data, regions may also suffer from a lack of paleomagnetic data for specific time intervals. This might be due to unknown lava flow ages or infrequent volcanic eruption intervals. Therefore, constructing a reliable PSV curve for volcanic islands, remote locations or in regions in the Southern Hemisphere often proves to be difficult.

Paleosecular variation curves are mostly constructed for the last thousands of years. The age of deposits within this period is sometimes known absolutely, but often they are dated with radiocarbon. The previous methods to construct PSV curves assumed the radiocarbon age uncertainty to be normally distributed (e.g., Thébault & Gallet, 2010). However, due to non-linear changes in the atmospheric $^{14}C/^{12}C$ ratio the calibrated age distribution may become very complex. Béguin et al. (2021) present a method to construct a PSV curve when data density is lower, which by using bootstrapping also takes the uncertainty in radiocarbon age into account. However, PSV curves reconstructed with the method of Béguin et al. (2021) still rely on simply connecting the available datapoints, which naturally results in greater uncertainties in declination, inclination and intensity in time intervals with less data.

21699356, 2026, 2, Downloaded from https://agupubs.onlinelibrary.wiley.com/doi/10.1029/2025JB032670, Wiley Online Library on [07/11/2026]. See the Terms and Conditions (https://onlinelibrary.wiley.com/terms-and-conditions) on Wiley Online Library for rules of use; OA articles are governed by the applicable Creative Commons License

In this study, we address this limitation by incorporating global geomagnetic field models as prior knowledge, which helps constrain the PSV curve in poorly sampled time intervals. This novel method to estimate PSV curves is especially aimed at regions with low paleomagnetic data coverage. Furthermore, we include the full radiocarbon age distribution, which reflects the dating uncertainties in the final model. We demonstrate the method using a synthetic data set, and ultimately with a case study implementing data from the Azores study of Béguin et al. (2021). Users may select from multiple global models or opt for a simple dipole-based prior. This provides an approach to construct local paleosecular variation curves for remote locations with limited available data.

2. Methods

We propose to construct local PSV curves based on a Gaussian process prior. If only a few datapoints are available locally, we suggest building the prior from an existing, global model. In the following, we describe the prior model, likelihood and inference strategy.

2.1. Brief Introduction to Gaussian Process Modeling

Here we present a brief overview of Gaussian process modeling. For a more extensive introduction, we highly recommend the book by Rasmussen and Williams (2006). Gaussian processes can be seen as the continuous generalization of multivariate normal distributions. They are uniquely defined by a mean function and a covariance function or kernel. For a random variable f one writes

$$f \sim \mathrm{GP}(\bar{f}, K_f),$$

where $\bar{f}$ is the mean function and K_f the kernel. As a stochastic process, f is continuous over a continuous set X, for example, time or the Earth's surface. For all finite vectors $\boldsymbol{x} = (x_1, \ldots, x_n)^\top$ where the x_i are in X, the vector $\boldsymbol{f}(\boldsymbol{x}) = (f(x_1), \ldots, f(x_n))^\top$ is a multivariate random variable with mean $\bar{\boldsymbol{f}}(\boldsymbol{x})$ and covariance matrix $\Sigma_{i,j} = K_f(x_i, x_j)$. Gaussian processes define distributions over function spaces. The properties of the functions (smoothness, amplitude, etc.) in this space are fixed by the kernel function. For additional information on the relation between function spaces and Gaussian processes, we recommend Berlinet and Thomas-Agnan (2004) and Kanagawa et al. (2018).

Within Bayesian inference, one can use a Gaussian process as a prior model. Let $o(z) = f(z) + \epsilon$ be observations at locations z with normally distributed measurement errors ϵ with covariance matrix Σ_o. Then the posterior is also a Gaussian process

$$f|o \sim \mathrm{GP}(\mathbb{E}[f(x)|o], \mathrm{Cov}[f(x), f(y)|o]),$$

with mean function

$$\mathbb{E}[f(x)|o] = \bar{f} + K_f(x,z)\left(K_f(z,z) + \Sigma_o\right)^{-1}\left(o - \bar{f}(z)\right) \tag{1}$$

and covariance function

$$\mathrm{Cov}[f(x), f(y)|o] = K_f(x,y) - K_f(x,z)\left(K_f(y,y) + \Sigma_o\right)^{-1} K_f(z,y). \tag{2}$$

Note that the posterior covariance does not depend on the observations o but only on the locations of observation y and the error covariance Σ_o. In the cases of archeo- and paleomagnetism, the magnetic field vector is not observed directly, but its intensity and/or directions are estimated based on preserved remanent magnetizations. Due to this non-linearity, standard Gaussian process regression as laid out here is not directly applicable and approximation techniques have to be employed (see Section 2.4). Nevertheless, central properties of the linear case persist also in the non-linear one.

Figure 1 shows an example of Gaussian process regression in an arbitrary, linear and one dimensional setting. From the right panel, one can see that records with large measurement uncertainties do not reduce the posterior

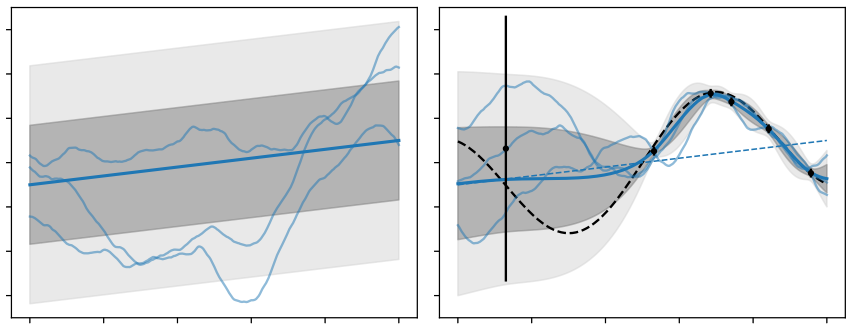


Figure 1. Basic example of Gaussian process regression. The left panel shows the prior. The mean function is drawn as a thick blue line, three samples from the prior are shown as thin lines. The right panel shows an arbitrary function as a black dashed line. Synthetic data, shown in black, has been generated from this function. The posterior mean, corresponding to this data and the prior of the left panel, is shown as a thick blue line, three posterior samples are shown as thin blue lines. For comparison, the prior mean is shown as a dashed line. In both panels, the shaded areas cover one and two point-wise standard deviations respectively.

uncertainties as much as records with smaller measurement uncertainties. In the left part of the right panel, the posterior mean is close to the prior. This is because the record does not add much information to the model.

2.2. Gaussian Process Prior

We employ Bayesian inference to construct a PSV curve at a location of interest. At this location, we model the geomagnetic field vector $\boldsymbol{B}$ with a Gaussian process prior

$$\boldsymbol{B}(t) \sim \mathrm{GP}\big(\bar{\boldsymbol{B}}(t), K(t,t')\big), \tag{3}$$

where $\bar{\boldsymbol{B}}(t)$ is the prior mean function and $K(t,t')$ the prior covariance kernel. Since $\boldsymbol{B}$ is a 3-dimensional vector, for every time t, $\bar{\boldsymbol{B}}(t)$ is a 3-dimensional vector as well and for every pair of times t and t', $K(t,t')$ is a 3×3 matrix. We distinguish three different approaches for choosing $\bar{\boldsymbol{B}}(t)$ and $K(t,t')$:

One option is to use a constant axial dipole field for the mean function $\bar{\boldsymbol{B}}(t)$. By default, the value of the axial dipole is set to -30 μT, an average value for the Holocene (e.g., Nilsson et al., 2022). It is straightforward to use a different value. A priori, the local vector components are assumed to be uncorrelated with a Matérn-covariance function

$$K_{ij}(t,t') = \sigma^2 \kappa_{ij} \delta_{ij} \cdot \left(1 + \frac{|t-t'|}{\tau}\right) \exp\left(-\frac{|t-t'|}{\tau}\right), \tag{4}$$

where δ_{ij} is the Kronecker delta, σ is the a priori standard deviation and τ the correlation time. κ_{ij} is introduced to address the magnetic field geometry and is one for the North and East component and two for the down component. Default values for σ (10 μT) and τ (150 yrs) were selected heuristically. The initial range of values was determined by the collection of different values used to construct recent statistical models (Hellio & Gillet, 2018; Nilsson et al., 2022; Schanner et al., 2022). We ran the code with σ between 5 and 15 μT and τ between 100 and 250 yrs. The chosen default values worked best to capture data variability in the presented case study. Similar to the axial dipole, the values can be changed easily, if for example, one wants to explicitly model faster or higher amplitude variations. The a priori model is anchored to the present day field by one inference step, in which the year 2000 prediction of the Kalmag model (Baerenzung et al., 2022) is included as an artificial observation. For the mean, this gives

$$\bar{\boldsymbol{B}}(t) = \boldsymbol{B}_{\mathrm{ax}} - \frac{K(t,t_{2000})}{\sigma^2} \cdot (\boldsymbol{B}_{2000} - \boldsymbol{B}_{\mathrm{ax}}), \tag{5}$$

21699356, 2026, 2, Downloaded from https://agupubs.onlinelibrary.wiley.com/doi/10.1029/2025JB032670, Wiley Online Library on [07/11/2026]. See the Terms and Conditions (https://onlinelibrary.wiley.com/terms-and-conditions) on Wiley Online Library for rules of use; OA articles are governed by the applicable Creative Commons License

21699356, 2026, 2, Downloaded from https://agupubs.onlinelibrary.wiley.com/doi/10.1029/2025JB032670, Wiley Online Library on [07/11/2026]. See the Terms and Conditions (https://onlinelibrary.wiley.com/terms-and-conditions) on Wiley Online Library for rules of use; OA articles are governed by the applicable Creative Commons License

where $\boldsymbol{B}_{\text{ax}}$ is the magnetic field vector of the axial dipole field at the location of interest and $\boldsymbol{B}_{2000}$ the field prediction of Kalmag for the epoch 2,000 at the location of interest. The covariance is updated analogously (Equation 2). We refer to this as the simple GAD prior (Geocentric Axial Dipole).

The simple option works well in situations where many records from a single location of interest are available, for example, in the common era Europe. In situations where data are sparse, we suggest to use a global field model posterior as a local prior. The PSV curve in this scenario is an update to the local model prediction, based on the new data. The prior mean function is directly available from the model ensemble, the local covariance is approximated by a multivariate Gaussian, as described below. We call these global model priors. Currently, four global models can be used as priors: pfm9k.2 (Nilsson et al., 2022), COV-ARCH (Hellio & Gillet, 2018), ArchKalmag14k.r (Schanner et al., 2022) and ArchKalmag8k (Schanner et al., 2025). Note that due to the way these models are constructed, uncertainties in the Southern Hemisphere are larger than in the Northern, as expected (see e.g. Figure 11 in Hellio and Gillet (2018)). To avoid the global models being overconfident we include the option to increase the model standard deviation by an arbitrary factor. By default, this factor is set to 1. A reviewer suggested to use only the large scale degrees as a prior. We therefore constructed an average model of the three ensembles, that can be truncated at large scales to use only global features that are part of all models. To address the undetermined small scale structures of the magnetic field, additional variance is added to the model according to the global statistical parameters determined by Schanner et al. (2025). We refer to this as the large scale prior. We investigate the influence of the choice of priors in Section 3.

2.3. Paleomagnetic Data

In paleomagnetism, indirect observations of the Earth's magnetic field are provided as declination D, inclination I and/or intensity F. They relate non-linearly to the magnetic field vector $\boldsymbol{B} = (B_N, B_E, B_Z)^\top$, where B_N is the North, B_E the East and B_Z the downward component. For the directions and intensity, the following functions define the relation between B_N, B_E, B_Z and D, I, and F:

$$D = \arctan\left(\frac{B_E}{B_N}\right) \tag{6}$$

$$I = \arctan\left(\frac{B_Z}{\sqrt{B_N^2 + B_E^2}}\right) \tag{7}$$

$$F = \sqrt{B_N^2 + B_E^2 + B_Z^2} \tag{8}$$

We model the measurement errors for all three (declination, inclination and intensity) by Student's $\mathcal{T}$-distributions with 4 degrees of freedom (we use $\mathcal{T}$ for the distribution, instead of the more common t, as the latter is used for the specimen ages). The wider tails of the $\mathcal{T}$-distribution compared to a normal distribution allow the model to better deal with inconsistencies in the data set. For the intensity measurements, the $\mathcal{T}$-distribution's scale parameter is set to the provided standard deviation σ_H. For the directions, the common approximations to the α_{95} confidence cone are used (e.g., Suttie & Nilsson, 2019).

$$\sigma_I = \frac{57.3}{140}\alpha_{95} \tag{9}$$

$$\sigma_D = \frac{\sigma_I}{\cos I} \tag{10}$$

Paleomagnetic data can be associated with one of four types of dating, each with their own uncertainty that needs to be considered in modeling. If the age of a unit is known precisely, often from a direct observation, it is included deterministically as a fixed number and from here on referred to as “absolutely dated”. If only the era of a sample is known, for example from a historical source or from stratigraphical bracketing between two units with known ages, the ages must be modeled as uniformly distributed within an interval. We call these “uniformly dated”:

$$t \sim \text{Uniform}(t_{\min},\ t_{\max}) \tag{11}$$

If a sample is associated with a radiocarbon age and both the radiocarbon age $\mu^{14}\text{C}$ and its uncertainty $\sigma^{14}\text{C}$ are available, we follow Blaauw and Christen (2011) to include the appropriate calibration curve in the model (Heaton et al., 2020; Hogg et al., 2020; Reimer et al., 2020). The nature of the radiocarbon calibration curve leads to a possibly highly multimodal distribution, which will be considered appropriately in our Bayesian approach.

$$\begin{aligned} t &\sim \mathcal{T}_3(\mu, 2\sigma), \\ \mu &= \mu_{^{14}\text{C}} - \mu_{\text{cal}}(t), \\ \sigma^2 &= \sigma^2_{^{14}\text{C}} + \sigma^2_{\text{cal}}(t). \end{aligned} \tag{12}$$

where $\mu_{\text{cal}}(t)$ and $\sigma_{\text{cal}}(t)$ are the mean and standard deviation of the calibration curve at time t. Lastly, we also include the option to model the ages as a normal distribution, for example, when the age of a volcanic unit is inferred from the growth of pioneer tree species (Albert et al., 2020), or if the radiocarbon age is pre-calibrated and the original data are not available.

Together, an observation o of the field vector $\boldsymbol{B}$ is modeled by

$$\begin{aligned} o(t) &= H[\boldsymbol{B}(t)] + \epsilon_H, \\ H \in \{D, I, F\}, &\qquad \epsilon_H \sim \mathcal{T}_4(0, \sigma_H), \\ t &\in \left\{t_{\text{fixed}}, t_{\text{uniform}}, t_{^{14}\text{C}}, t_{\text{normal}}\right\}. \end{aligned} \tag{13}$$

Together, these components define the likelihood of our Bayesian PSV-curve.

2.4. Hamiltonian Monte-Carlo Inference

The non-linearity of the observation functionals H and the random variable nature of the observation ages t make the posterior inaccessible in closed form. It is possible to approximate the posterior by using normal distributions for the ages and by linearizing the observation functionals (McHutchon & Rasmussen, 2011; Schanner et al., 2021). Instead, we consider the non-linearity and the full form of the age distributions in the posterior, by generating a posterior ensemble using Hamiltonian Monte-Carlo inference (e.g., Betancourt, 2018).

To speed up the sampling, we use two minor approximations. The first one relates to the multimodal radiocarbon age models. Instead of considering the time continuous distribution (12), we evaluate (12) at the calibration curve knot points and return a discrete distribution at points where the probability is above a threshold of 10^{-3}. This is similar to `Bchron` (Haslett & Parnell, 2008). For sampling, the actual distribution (12) is then approximated by inverse cdf-sampling and linear interpolation. For a single data point, we tested sampling the approximate and full distribution and found no significant difference in the posterior ensemble. The sampling speed was about two orders of magnitude faster with the approximation. The second approximation concerns the Gaussian process. The ensemble models are already provided at specific knot points, that, is as realizations of the Gaussian process posterior. These form a multivariate normal distribution. Instead of trying to recover the actual Gaussian process functions, we adopt the multivariate normal approximation and linearly interpolate between the knot points. At the cost of minor inaccuracies, this prevents expensive calls to the kernel function at the random ages. Further, this reduces calculating the a priori correlation function from the ensemble to calculating the ensemble covariance matrix.

We implement the described model using the probabilistic programming language `PyMC` (Abril-Pla et al., 2023). `PyMC` provides a high-level interface to a wide range of probability distributions, that can be combined to reflect complex models, such as the one presented here. It also provides high level access to an efficient No-U-Turn Sampler (NUTS Hoffman & Gelman, 2014), as well as just-in-time compilation (Bradbury et al., 2018). Our implementation is provided as a python package and comes with tutorial notebooks, showcasing how to use it. The code is available on GitHub https://github.com/arthus701/pypsv.

21699356, 2026, 2, Downloaded from https://agupubs.onlinelibrary.wiley.com/doi/10.1029/2025JB032670, Wiley Online Library on [07/11/2026]. See the Terms and Conditions (https://onlinelibrary.wiley.com/terms-and-conditions) on Wiley Online Library for rules of use; OA articles are governed by the applicable Creative Commons License

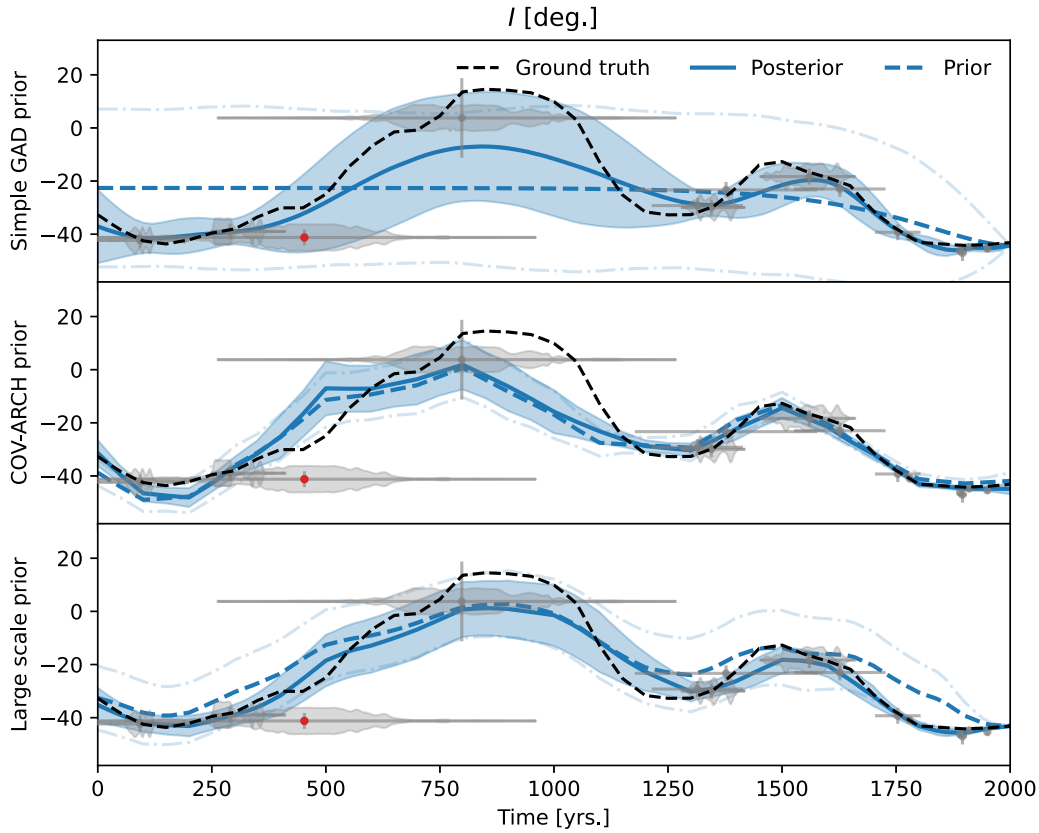


Figure 2. Inclination component of synthetic PSV curves for the Comoros, generated with our model using different priors. The solid blue lines depict the posterior mean, the shaded area covers one point-wise standard deviation of the posterior. The dashed blue line shows the prior mean, the dash dotted lines indicate one point-wise standard deviation of the prior. The dashed black line depicts the ground truth, a sample from the pfm9k.2 model, used to generate the synthetic data, shown in gray. The violins indicate the multi-modal age distributions from radiocarbon dating. The prior and posterior age distributions for the record highlighted by the red dot are shown in Figure 4.

3. Validation

To validate the proposed method, we construct a synthetic data set for the Comoros. The Comoros is a volcanic archipelago, located between Africa and Madagascar. Data coverage is sparse there, which is why it is well suited as a test location. We use a sample from the pfm9k.2 model ensemble (Nilsson et al., 2022), to generate declination, inclination and intensity data at the location of Mount Karthala on Ngazidja (Grande Comore; 11.78° S, 43.35° E). We choose specific input dates and treat some of the data as radiocarbon, some as uniformly and some as absolutely dated. According to specified error levels, a random shift in age is added to the input dates and artificial, normally distributed measurement errors are added to the generated declination, inclination and intensity. For some records, we specifically set the values to illustrate the behavior of our Bayesian modeling procedure. We then run our model on the data, using the simple GAD prior, a prior generated from the COV-ARCH model (Hellio & Gillet, 2018) and the large scale prior with truncation degree 2 (see Section 2.2). Note that COV-ARCH and pfm9k.2 share parts of the data set, so the COV-ARCH prior is already close to the ground truth in this synthetic example. The same is true for the large scale prior, as it is constructed from both pfm9k.2 and COV-ARCH.

Figure 2 shows the reconstructed local inclination curves for the three cases. Declination and intensity curves are similar and presented in the appendix (Figures A1 and A2). For the recent centuries, up until ca. 1300 CE, all models are able to capture the reference signal. Because the original COV-ARCH model and the reference process agree well for this time, the reconstruction using the COV-ARCH prior is slightly better. Differences are found for earlier times. During the intermediate period, between 600 and 1250 CE, the simple GAD prior is drawn to the poor quality record. For the COV-ARCH and large scale priors, the poor quality record is close to their prior, so

21699356, 2026, 2, Downloaded from https://agupubs.onlinelibrary.wiley.com/doi/10.1029/2025JB032670, Wiley Online Library on [07/11/2026]. See the Terms and Conditions (https://onlinelibrary.wiley.com/terms-and-conditions) on Wiley Online Library for rules of use; OA articles are governed by the applicable Creative Commons License

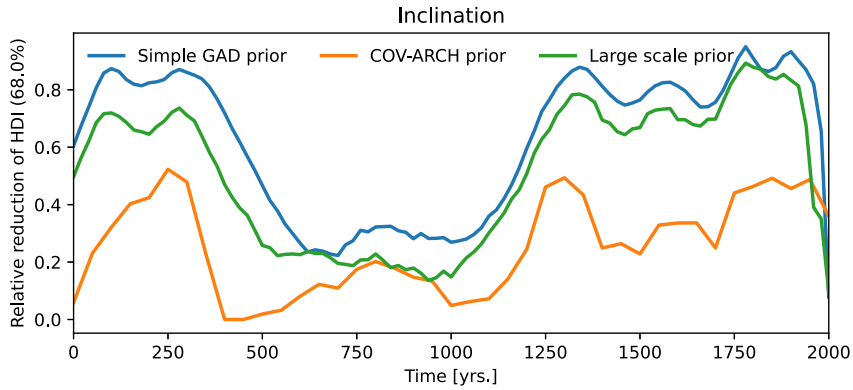


Figure 3. Relative reduction of the widths of the point-wise 68% highest density intervals for the inclination curves of the synthetic case. The corresponding prior and posterior curves are presented in Figure 2.

the model does not change substantially. For the earlier times, 0 CE to 300 CE, there are three datapoints, two of which are dated quite well and one, that is, not very well dated. The simple GAD prior gives a wide plateau for these times, while due their priors, the other two models reproduce the bend of the true signal. Likely due to larger a priori variance, the large scale prior is able to capture the true signal better than the COV-ARCH prior. Comparing prior and posterior mean functions only gives part of the picture of Bayesian inversion. The shaded area in Figure 2 shows one point-wise standard deviation of the posterior, the dash-dotted lines indicate the same for the prior.

To better visualize the change from prior to posterior, Figure 3 shows the relative reduction of the point-wise 68% highest density intervals (HDIs). The larger the value, the more the spread of the posterior compared to the prior distribution is reduced at the given point in time. As the COV-ARCH prior is already quite confident for the early times, the reduction is lower for this model. The plateau between 500 and 1000 CE indicates, that the poor quality record does not add much information to the model. The same is true for the record from 414 CE, shown in red in Figure 2. Even though for this record the inclination is relatively well determined, due to the large error in dating, the record does not add much information to the model. Instead, the age distribution for this record is updated by the model. Figure 4 shows the prior and posterior age distribution for this record. Because there are two better dated records to the left of it, even the simple GAD prior model shifts the age of the record. Because of the more informative priors, the shift is stronger for the other two models, and especially for COV-ARCH.

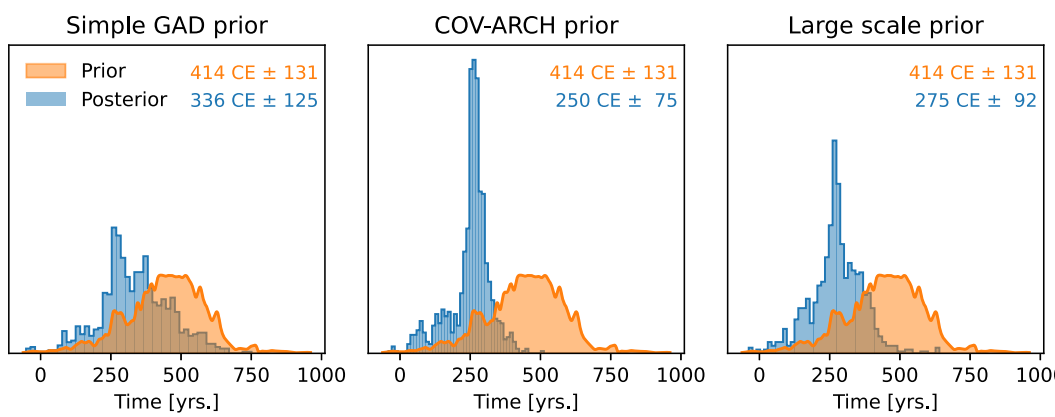


Figure 4. Prior and posterior distribution of the age of the red highlighted synthetic record in Figure 2. The numbers in the top right corners indicate mean and one standard deviation of the respective distributions. The true age of the synthetic record is 218 CE.

21699356, 2026, 2, Downloaded from https://agupubs.onlinelibrary.wiley.com/doi/10.1029/2025JB032670, Wiley Online Library on [07/11/2026]. See the Terms and Conditions (https://onlinelibrary.wiley.com/terms-and-conditions) on Wiley Online Library for rules of use; OA articles are governed by the applicable Creative Commons License

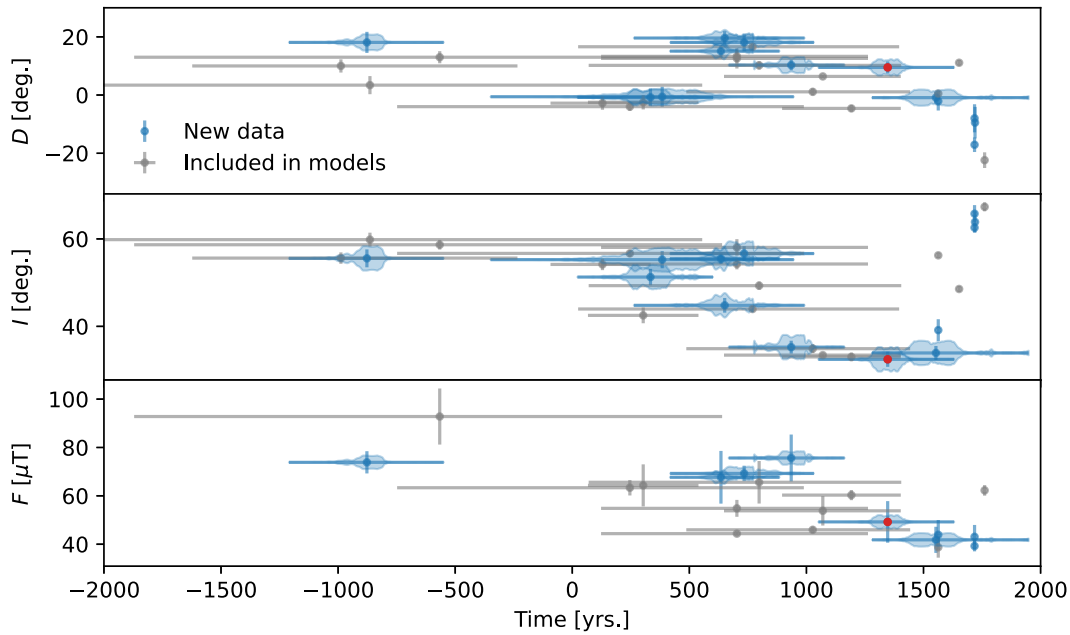


Figure 5. Declination D, inclination I and intensity F data from the Azores. The spatial distribution is depicted in Figure 6. Inclination and intensity data have been translated to a common latitude (e.g., Merrill et al., 1996). Gray data are included in the GEOMAGIA database (Brown et al., 2021) and thereby in the global models we consider. Blue data are new, in this sense (Béguin et al., 2021). For the new data, the age distributions are depicted as violins. Data points without horizontal error bars are absolutely dated. Sample PI5 is highlighted in red.

4. Case Study

We present an example case study of the proposed PSV curve construction method. For the Azores, many data points are available. Some of these records were used to construct the ArchKalmag14k.r (Schanner et al., 2022) and pfm9k.2 (Nilsson et al., 2022) models. For illustration purposes and to avoid circular reasoning, we construct PSV curves based only on data that were not used in the models.

The Azores data set is depicted in Figure 5. Data from Béguin et al. (2021) that are not included in the GEOMAGIA database (Brown et al., 2021), and therefore not in the global models we consider as priors, is depicted in

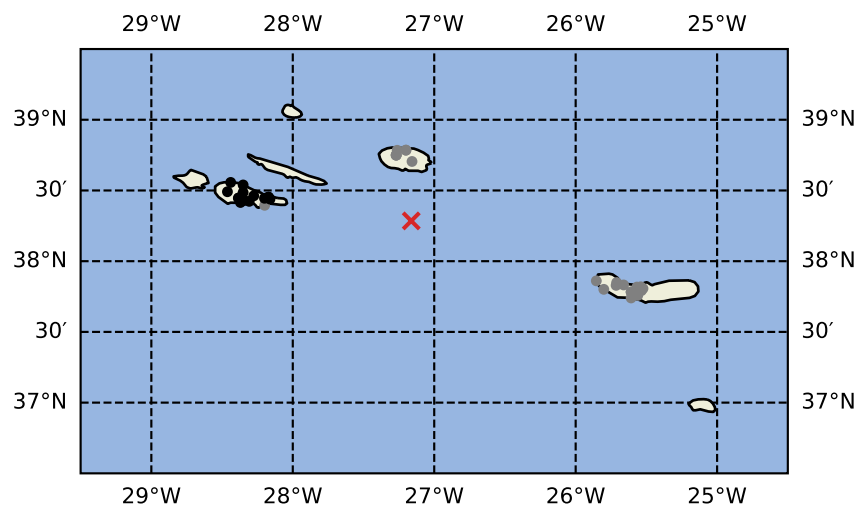


Figure 6. Spatial distribution of the Azores data set. Gray data are included in the GEOMAGIA database (Brown et al., 2021) and thereby in the global models we consider. Black data are new, in this sense (Béguin et al., 2021). The red cross marks the location for which the PSV curves are constructed.

21699356, 2026, 2, Downloaded from https://agupubs.onlinelibrary.wiley.com/doi/10.1029/2025JB032670, Wiley Online Library on [07/11/2026]. See the Terms and Conditions (https://onlinelibrary.wiley.com/terms-and-conditions) on Wiley Online Library for rules of use; OA articles are governed by the applicable Creative Commons License

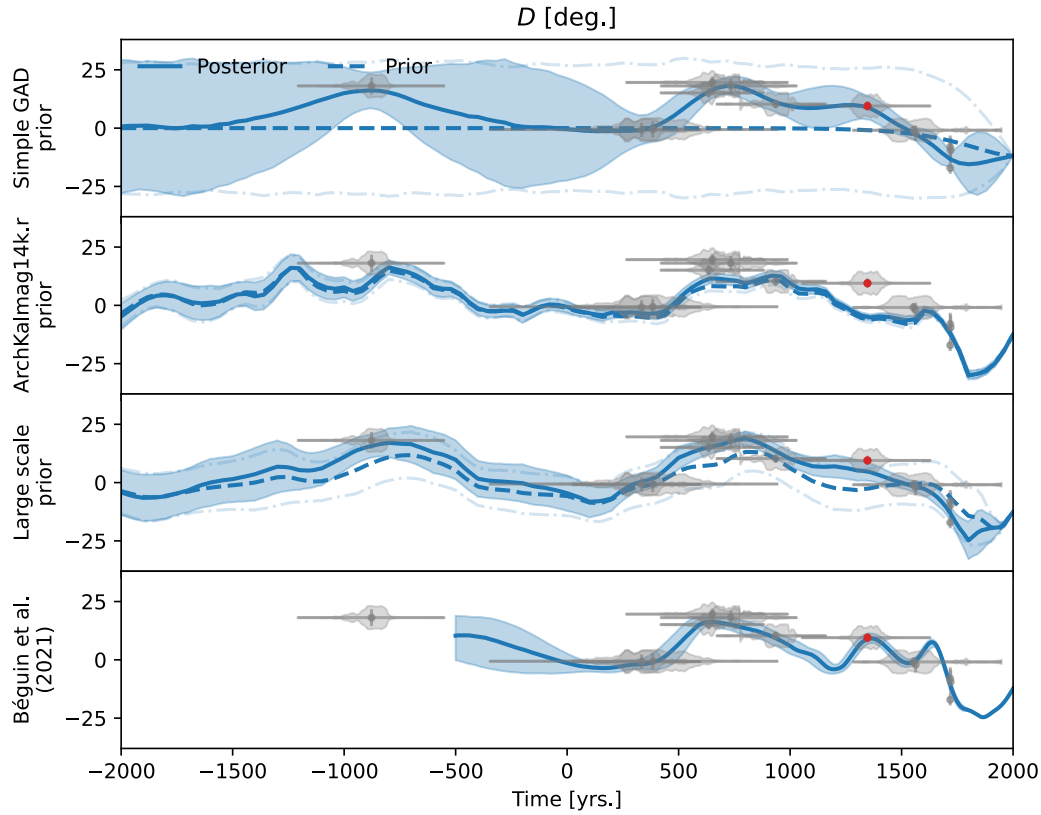


Figure 7. Declination component of the PSV curves, generated with our model using different priors for the Azores. The solid blue lines depict the posterior mean, the shaded area covers one point-wise standard deviation. The dashed blue line shows the prior mean, the dash-dotted line one point-wise prior standard deviation. Gray data from Béguin et al. (2021) are not included in the GEOMAGIA database. Sample PI5 is highlighted by a red dot. The bottom panel shows the PSV curve produced by Béguin et al. (2021), together with a 68% confidence interval.

blue. If the age of a data point is determined using radiocarbon dating, we depict the resulting multi-modal distribution by a violin plot. In general, the blue data points are consistent with the data, that is, already included in GEOMAGIA (depicted in gray). However, especially in the inclination around 1500 CE, some data are inconsistent or hint at very rapid field changes. The spatial distribution of the data are shown in Figure 6. In the following, we discuss PSV curves for the location marked by a red cross in Figure 6 (38.28° N, 27.16° W).

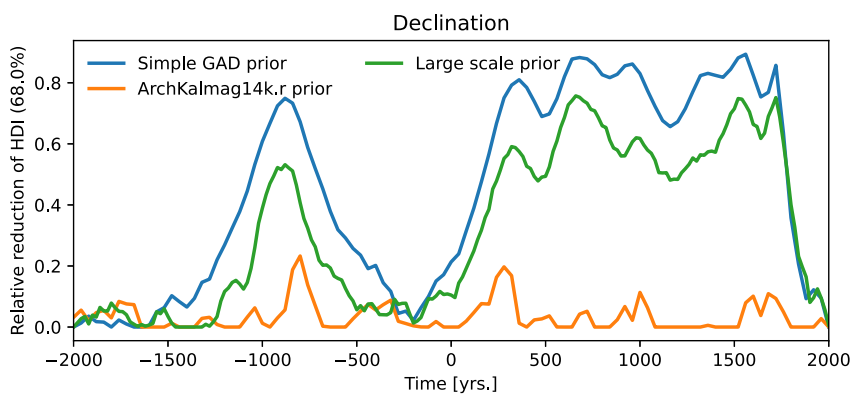


Figure 8. Relative reduction of the widths of the point-wise 68% highest density intervals for the declination of the Azores case study. The corresponding prior and posterior curves are presented in Figure 7.

21699356, 2026, 2, Downloaded from https://agupubs.onlinelibrary.wiley.com/doi/10.1029/2025JB032670, Wiley Online Library on [07/11/2026]. See the Terms and Conditions (https://onlinelibrary.wiley.com/terms-and-conditions) on Wiley Online Library for rules of use; OA articles are governed by the applicable Creative Commons License

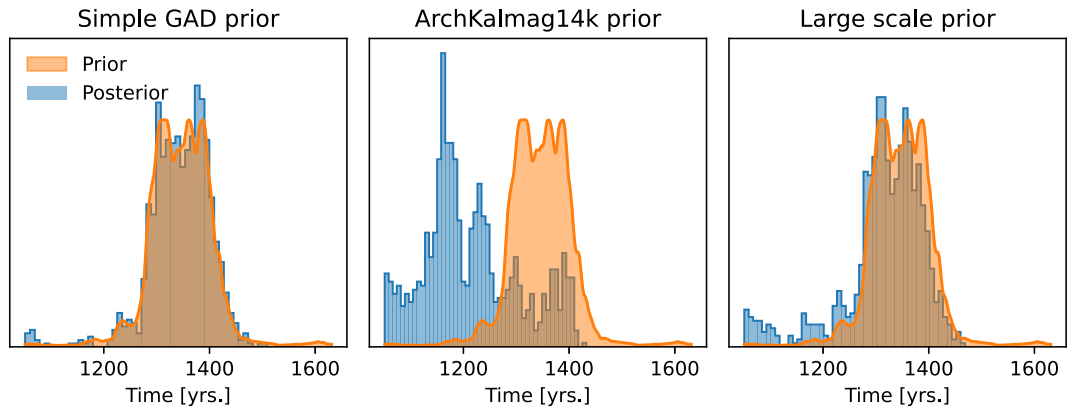


Figure 9. Prior and posterior age distributions for sample PI5. In Figures 5 and 7, sample PI5 is highlighted by a red dot.

We construct three curves. The first curve is based on the simple GAD prior. The second curve uses the local prediction of the global ArchKalmag14k.r model as a prior, and updates the prediction with the data. The third curve uses the large scale prior, truncated at degree two. Our modeling code was used to sample the posterior distribution for the three different curves. After a tune-in phase of 1,000 steps, 4 chains of 500 samples were generated for each curve. The final chains indicate good mixing and low auto-correlation. A tail estimate of the mean effective sample size ratio was 0.73 for the first, 0.70 for the second and 0.72 for the third curve. The $\hat{R}$ statistic, which compares the in chain variance with the between chain variance (Vehtari et al., 2021), was below 1.1 for all random variables. This indicates good convergence.

Figure 7 shows the posterior declination curves. The figures for inclination and intensity are similar and presented in the appendix (Figures B1 and B2). For the simple GAD prior, the a priori mean is a straight line, that goes to the modern value (dashed line in the top panel). The posterior mean (solid line in the top panel) fits the data well. The point-wise posterior standard deviation, depicted with light blue shading, indicates reduced uncertainties for epochs of good data coverage. For the ArchKalmag prior, the posterior mean (solid line in the second panel) only slightly deviates from the prior mean (dashed line). This is due to the surrounding data from the Azores, which is already included in the model, and the large amount of data from Europe that exists for the last two millennia. The large scale prior (dashed line in the third panel) shows more structure than the simple GAD prior, but larger a priori standard deviation than ArchKalmag14k.r (dash-dotted lines). Therefore, the posterior mean is shifted more than for the global model. Similar to the validation, Figure 8 shows the relative reduction of the point-wise 68% HDIs for the three curves. From this figure, it becomes clear that the ArchKalmag14k.r posterior mainly reproduces the prior. For the other two models, this is also the case for the data gap between 0 CE and −1000 CE,

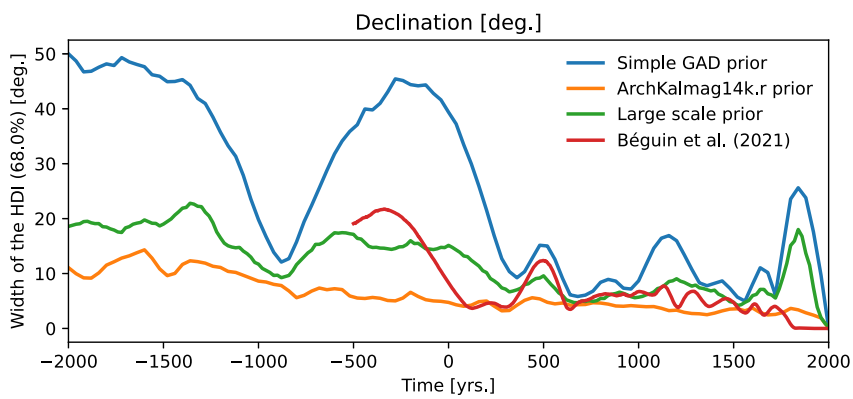


Figure 10. Width of the point-wise 68% highest density intervals for the declination of the Azores case study. The corresponding prior and posterior curves are presented in Figure 7.

21699356, 2026, 2, Downloaded from https://agupubs.onlinelibrary.wiley.com/doi/10.1029/2025JB032670, Wiley Online Library on [07/11/2026]. See the Terms and Conditions (https://onlinelibrary.wiley.com/terms-and-conditions) on Wiley Online Library for rules of use; OA articles are governed by the applicable Creative Commons License

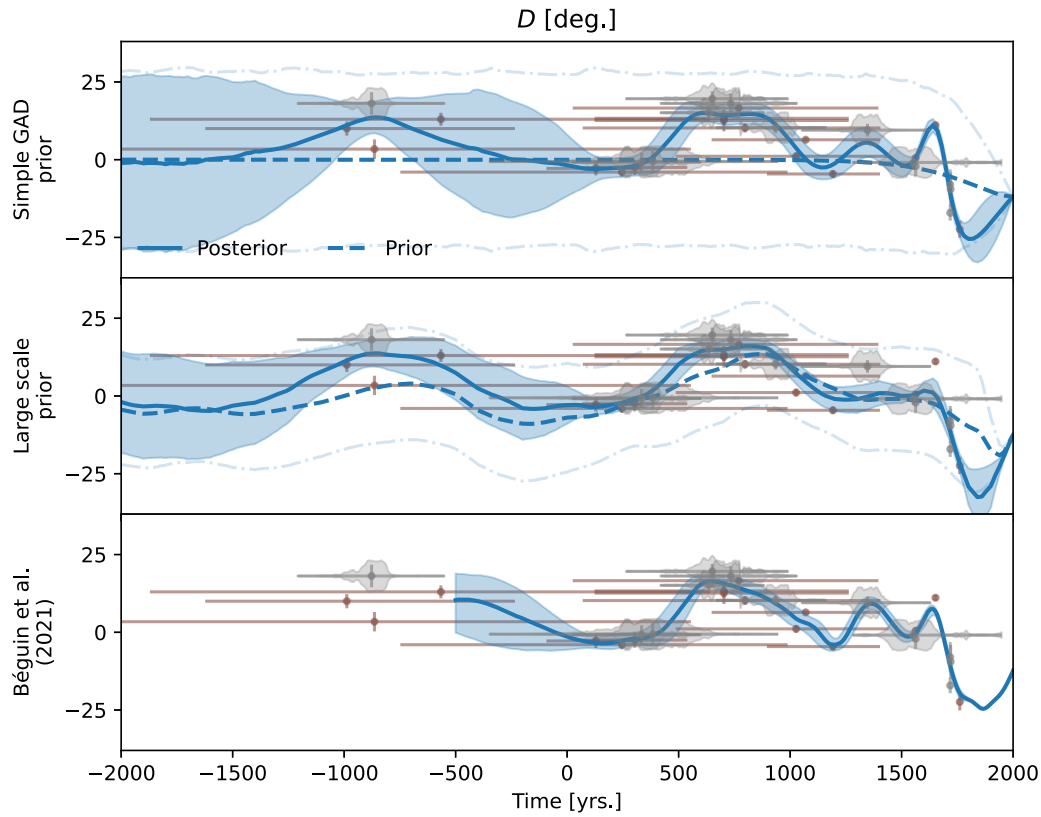


Figure 11. Declination component of the PSV curves, generated with our model using different priors and all available data for the Azores. The solid blue lines depict the posterior mean, the shaded area covers one point-wise standard deviation. The dashed blue line shows the prior mean, the dash-dotted line one point-wise prior standard deviation. Gray data from Béguin et al. (2021) is not included in the GEOMAGIA database. Brown data are taken from GEOMAGIA (Brown et al., 2021). The bottom panel shows the PSV curve produced by Béguin et al. (2021), together with a 68% confidence interval. Note that the model in the top panel did not converge. See the text for additional details.

while for the simple GAD prior, the interval where the prior is reproduced is shorter. A comparison to the data, shown in gray in Figure 7, reveals, that the ArchKalmag14k.r based curve does not fit all records. This is most obvious for the record with ID PI5, which is highlighted by a red dot. Figure 9 shows prior and posterior age distributions for this sample and the three models. In the ArchKalmag14k.r model, the age is shifted to agree with the prior.

The bottom panel of Figure 7 shows the reconstruction of Béguin et al. (2021), together with 68% confidence intervals. Around 1500 CE their curve shows more variability than the models we produced, due to the additional records shown in Figure 5, which were not included in our reconstructions. The ArchKalmag14k.r prior includes these data and indicates a swing similar to the curve of Béguin et al. (2021), but with smaller amplitude. Figure 10 shows the widths of the point-wise posterior 68% HDIs for the four curves. The intervals estimated by Béguin et al. (2021) with a bootstrap approach are in a comparable order of magnitude to the large scale model we constructed. However, their approach can not reflect correlations between the records, nor updates to the age distribution based on such correlations or prior information. Further, similar to the choice of prior in our approach, the estimate depends on the parameters used to construct the smoothing spline solutions.

4.1. Fitting All Data

Figure 11 shows two reconstructions based on all available data. The top panel uses the simple GAD prior, the center panel the large scale prior, again truncated at degree one. The bottom panel shows the reconstruction of

21699356, 2026, 2, Downloaded from https://agupubs.onlinelibrary.wiley.com/doi/10.1029/2025JB032670, Wiley Online Library on [07/11/2026]. See the Terms and Conditions (https://onlinelibrary.wiley.com/terms-and-conditions) on Wiley Online Library for rules of use; OA articles are governed by the applicable Creative Commons License

21699356, 2026, 2, Downloaded from https://agupubs.onlinelibrary.wiley.com/doi/10.1029/2025JB032670, Wiley Online Library on [07/11/2026]. See the Terms and Conditions (https://onlinelibrary.wiley.com/terms-and-conditions) on Wiley Online Library for rules of use; OA articles are governed by the applicable Creative Commons License

Béguin et al. (2021). For the simple GAD prior, the model does not converge. This is indicated by large $\hat{R}$ values, especially for the times between 500 CE and 1000 CE. In this interval, many records with large dating uncertainties lead to multimodality in the posterior, that can not be captured well with the employed algorithm. The large scale prior works better, but it already includes information from the additional records via the global models, leading to circular reasoning. It is interesting to note, that the model built from the large scale prior does not fit the record at 1563 CE and therefore does not show the swing that the other two models show.

5. Discussion and Outlook

We present a novel, Bayesian method of constructing PSV curves. This method allows the use of all available types of dating, and offers flexibility in the choice of the prior, by using a simple GAD prior or a global model prior. A simple GAD prior is sufficient in regions with dense data coverage, such as Europe. In regions with low data coverage, using a global geomagnetic field model as a prior is a valuable alternative to construct a more reliable PSV curve.

In comparison to the method proposed by Livermore et al. (2018), the method uses a much simpler prior structure based on Gaussian processes. Similar to the transdimensional approach proposed by Livermore et al. (2018), the Gaussian process can vary quickly in times of high data coverage and slowly if no data are present (see the top panel of Figure 7). The Gaussian process structure allows incorporating global models as an alternative prior. For regions of low data coverage, using a global model can improve the representation of the local field variability. This however comes with one obvious drawback: Regions of low data coverage are also the regions in which the global models are least reliable. Especially in the Southern Hemisphere, some global models show signs of overswinging, resulting in spurious signals. Further, for recent times, global models may be overconfident in regions of large data coverage. This is indicated by the curve in the second panel of Figure 9 not fitting the highlighted record. Instead, its age is shifted to agree with the prior. Which one is true (correcting the curve or shifting the age) can not be decided within the framework presented here. It is the responsibility of the investigator to select a prior they deem appropriate. Nevertheless, diagnosis like the reduction of uncertainties from prior to posterior (Figure 8) can help with the decision. In the presented case study, the curve based on the global model prior basically reproduces the prior. This can indicate consistency of the regional data with the global model, but may also indicate overconfidence, as described above. Especially in the presented case, dating uncertainties are large, and consistency with the prior does not relate to the quality of the data. We include multiple global models with our method, so that users can compare results from different models and assess the quality of the local reconstruction that way. If using a global model as a prior, one should take care that data used to construct the PSV-curve has not already been used to construct the model, to avoid circular reasoning. We also include the option to only use large scale information from the global models, by truncating a model constructed from all included ensembles at low spherical harmonics degree. This can mitigate the overconfidence, but still improve curve reconstruction compared to a simple axial dipole.

A strength of the proposed method is the explicit modeling of complex age distributions. By using modern Hamiltonian Monte-Carlo methods, strongly multimodal distributions, resulting from radiocarbon dating, can be incorporated. The resulting uncertainties are reflected in the reconstructed PSV curve. In contrast to the bootstrap approach, proposed by Béguin et al. (2021), the model can utilize cross correlations and prior information. Especially if dating uncertainties are large compared to the uncertainties in the magnetic signal, the method will update the age model instead of the PSV signal.

The method may be extended to reflect additional constraints, like ordered dates resulting from stratigraphy in archeological sites or lava flows. The proposed algorithm is implemented as a python package and distributed via GitHub https://github.com/arthus701/pypsv.

Appendix A: Additional Curves From Validation

Figure A1.

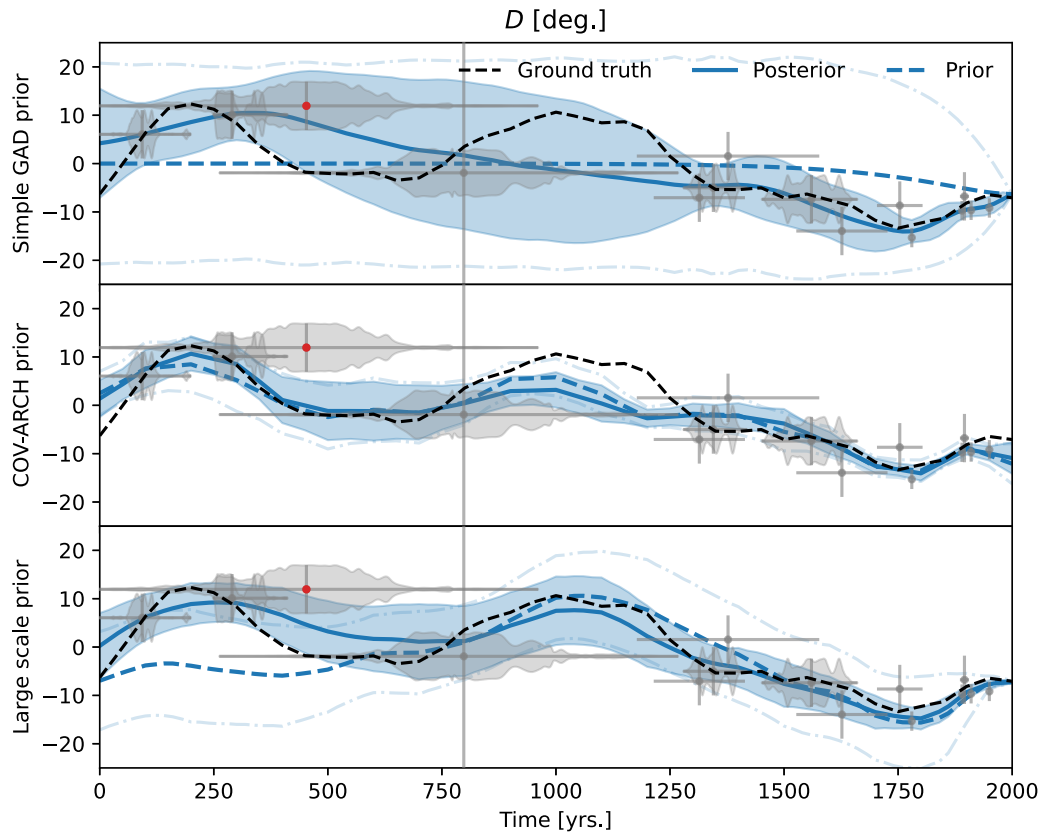


Figure A1. Declination component of synthetic PSV curves for the Comoros, generated with our model using different priors. The solid blue lines depict the posterior mean, the shaded area covers one point-wise standard deviation of the posterior. The dashed blue line shows the prior mean, the dash dotted lines indicate one point-wise standard deviation of the prior. The dashed black line depicts the ground truth, a sample from the pfm9k.2 model, used to generate the synthetic data, shown in gray. The violins indicate the multi-modal age distributions from radiocarbon dating. The prior and posterior age distributions for the record highlighted by the red dot are shown in Figure 4.

21699356, 2026, 2, Downloaded from https://agupubs.onlinelibrary.wiley.com/doi/10.1029/2025JB032670, Wiley Online Library on [07/11/2026]. See the Terms and Conditions (https://onlinelibrary.wiley.com/terms-and-conditions) on Wiley Online Library for rules of use; OA articles are governed by the applicable Creative Commons License

Figure A2.

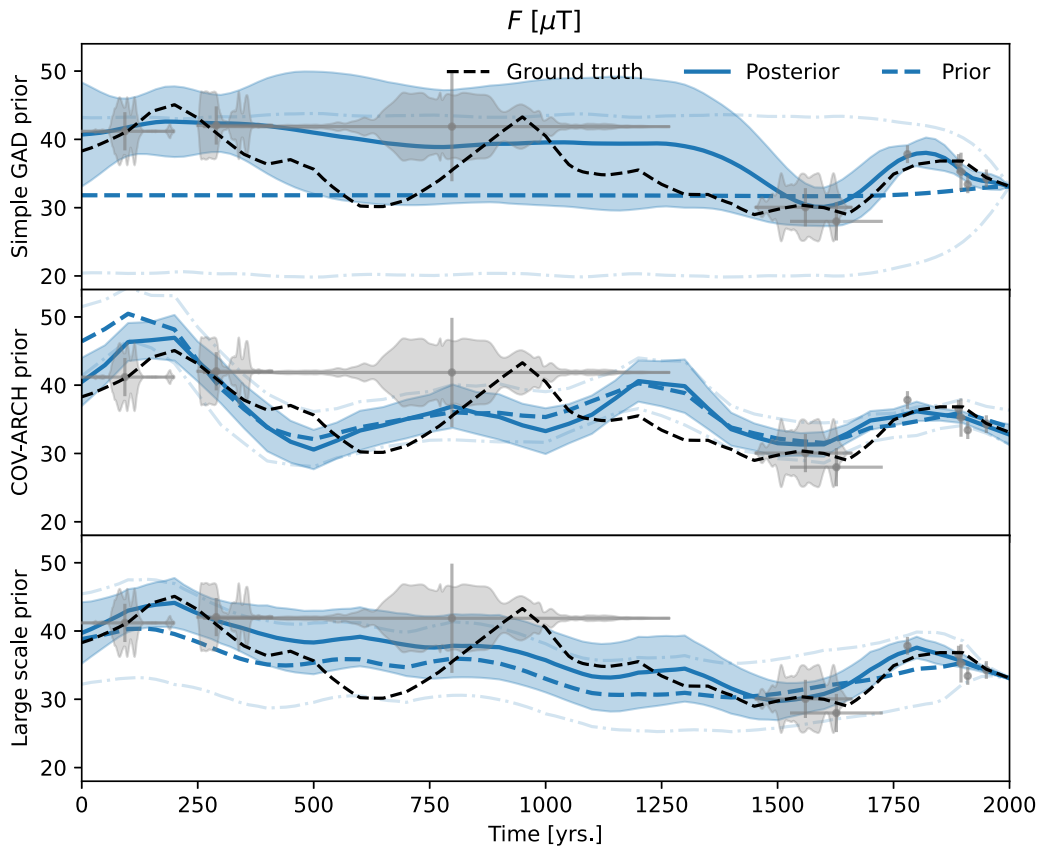


Figure A2. Intensity component of synthetic PSV curves for the Comoros, generated with our model using different priors. The solid blue lines depict the posterior mean, the shaded area covers one point-wise standard deviation of the posterior. The dashed blue line shows the prior mean, the dash dotted lines indicate one point-wise standard deviation of the prior. The dashed black line depicts the ground truth, a sample from the pfm9k.2 model, used to generate the synthetic data, shown in gray. The violins indicate the multi-modal age distributions from radiocarbon dating. The prior and posterior age distributions for the record highlighted by the red dot are shown in Figure 4.

21699356, 2026, 2, Downloaded from https://agupubs.onlinelibrary.wiley.com/doi/10.1029/2025JB032670, Wiley Online Library on [07/11/2026]. See the Terms and Conditions (https://onlinelibrary.wiley.com/terms-and-conditions) on Wiley Online Library for rules of use; OA articles are governed by the applicable Creative Commons License

Appendix B: Additional Curves From the Case Study

Figure B1.

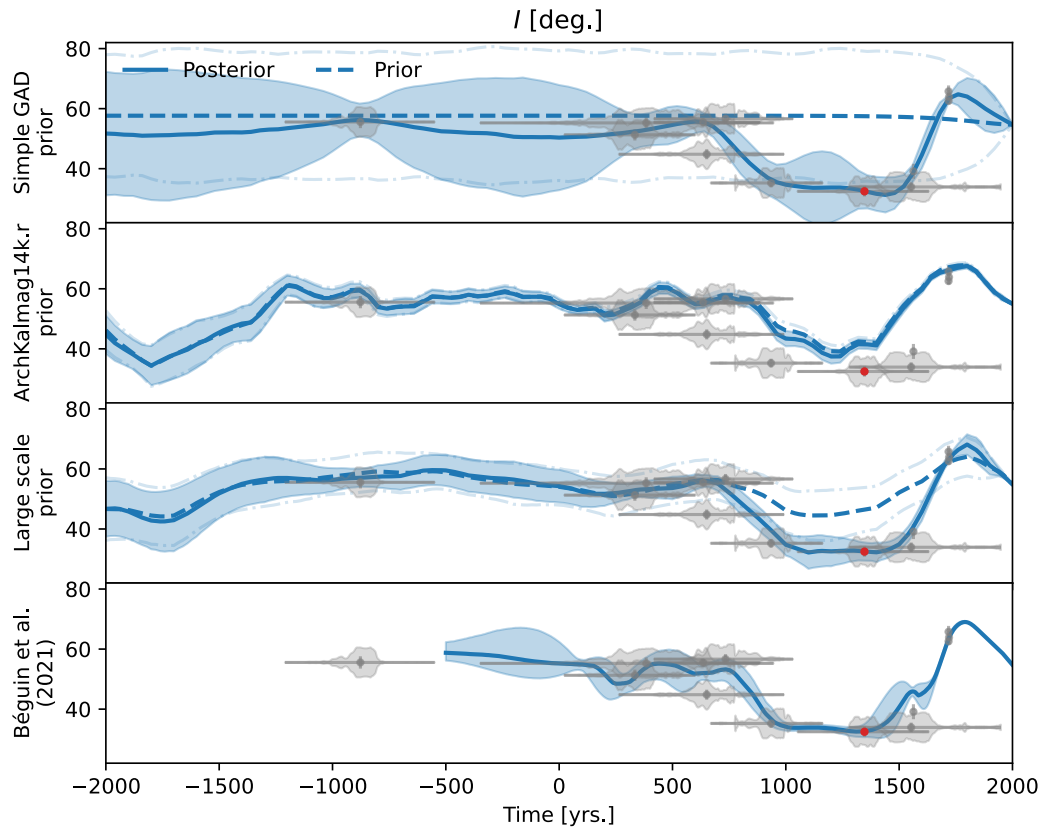


Figure B1. Inclination component of the PSV curves, generated with our model using different priors for the Azores. The solid blue lines depict the posterior mean, the shaded area covers one point-wise standard deviation. The dashed blue line shows the prior mean, the dash-dotted line one point-wise prior standard deviation. Gray data from Béguin et al. (2021) is not included in the GEOMAGIA database. Sample PI5 is highlighted by a red dot. The bottom panel shows the PSV curve produced by Béguin et al. (2021), together with a 68% confidence interval.

21699356, 2026, 2, Downloaded from https://agupubs.onlinelibrary.wiley.com/doi/10.1029/2025JB032670, Wiley Online Library on [07/11/2026]. See the Terms and Conditions (https://onlinelibrary.wiley.com/terms-and-conditions) on Wiley Online Library for rules of use; OA articles are governed by the applicable Creative Commons License

21699356, 2026, 2, Downloaded from https://agupubs.onlinelibrary.wiley.com/doi/10.1029/2025JB032670, Wiley Online Library on [07/11/2026]. See the Terms and Conditions (https://onlinelibrary.wiley.com/terms-and-conditions) on Wiley Online Library for rules of use; OA articles are governed by the applicable Creative Commons License

Figure B2.

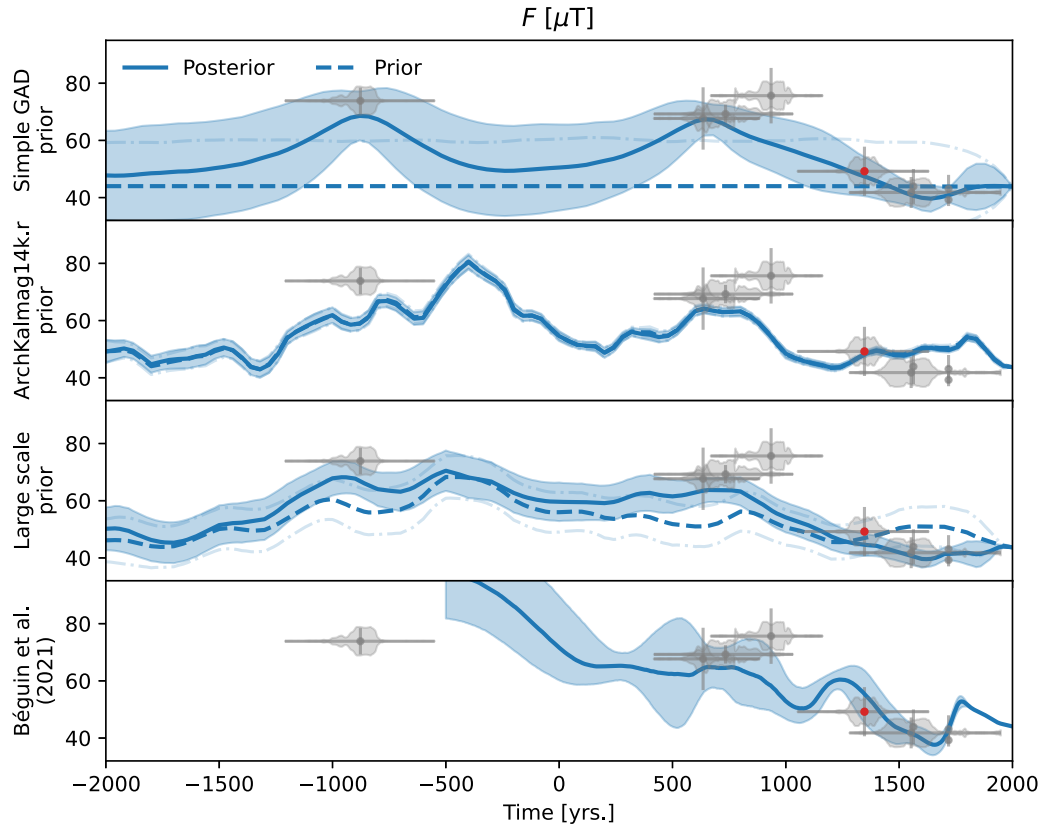


Figure B2. Intensity component of the PSV curves, generated with our model using different priors for the Azores. The solid blue lines depict the posterior mean, the shaded area covers one point-wise standard deviation. The dashed blue line shows the prior mean, the dash-dotted line one point-wise prior standard deviation. Gray data from Béguin et al. (2021) is not included in the GEOMAGIA database. Sample PI5 is highlighted by a red dot. The bottom panel shows the PSV curve produced by Béguin et al. (2021), together with a 68% confidence interval.

Conflict of Interest

The authors declare no conflicts of interest relevant to this study.

Data Availability Statement

The modeling software is released via GitHub. An archived version is available from Schanner (2025). The synthetic data set used for validation has been generated using pymagglobal (Schanner et al., 2020) and supplementary material from Hellio and Gillet (2018). The Azores data are available as a supplement to Béguin et al. (2021). Other paleomagnetic data that has been used is available via GEOMAGIA (Brown et al., 2021).

Acknowledgments
The authors want to thank two anonymous reviewers for extensive and helpful comments. We especially value the suggestion to explore the large scale prior model. MAS acknowledges funding by the German Research Foundation (DFG, Deutsche Forschungsgemeinschaft), Grant 388291411 and by the Helmholtz association within the Changing Earth InnoPool project "SOLVe". RM acknowledges funding by the Dutch Science Foundation (NWO): VIDI Grant VI. Vidi.192.047. Open Access funding enabled and organized by Projekt DEAL.

References

Abril-Pla, O., Andreani, V., Carroll, C., Dong, L., Fonnesbeck, C. J., Kochurov, M., et al. (2023). PyMC: A modern, and comprehensive probabilistic programming framework in Python. *PeerJ Computer Science*, *9*, e1516. https://doi.org/10.7717/peerj-cs.1516

Albert, S., Flores, O., Michon, L., & Strasberg, D. (2020). Dating young (<1000 yr) lava flow eruptions of Piton de la Fournaise volcano from size distribution of long-lived pioneer trees. *Journal of Volcanology and Geothermal Research*, *401*, 106974. https://doi.org/10.1016/j.jvolgeores.2020.106974

Baerenzung, J., Holschneider, M., Saynisch-Wagner, J., & Thomas, M. (2022). Kalmag: A high spatio temporal model of the geomagnetic field. *Earth Planets and Space*, *74*(139), 139. https://doi.org/10.1186/s40623-022-01692-5

Béguin, A., Pimentel, A., & de Groot, L. V. (2021). Full-Vector paleosecular variation curve for the azores: Enabling reliable paleomagnetic dating for the past 2 kyr. *Journal of Geophysical Research: Solid Earth*, *126*(2), e2020JB019745. https://doi.org/10.1029/2020JB019745

Berlinet, A., & Thomas-Agnan, C. (2004). *Reproducing kernel Hilbert spaces in probability and statistics*. Springer.

Betancourt, M. (2018). A conceptual introduction to hamiltonian Monte Carlo. https://doi.org/10.48550/arXiv.1701.02434

Blaauw, M., & Christen, J. A. (2011). Flexible paleoclimate age-depth models using an autoregressive gamma process. *Bayesian Analysis*, *6*(3), 457–474. https://doi.org/10.1214/11-BA618

Böhnel, H., Pavón-Carrasco, F. J., Sieron, K., & Mahgoub, A. N. (2016). Palaeomagnetic dating of two recent lava flows from Ceboruco volcano, western Mexico. *Geophysical Supplements to the Monthly Notices of the Royal Astronomical Society*, *207*(2), 1203–1215. https://doi.org/10.1093/gji/ggw310

Bradbury, J., Frostig, R., Hawkins, P., Johnson, M. J., Leary, C., Maclaurin, D., et al. (2018). JAX: Composable transformations of Python+NumPy programs. Retrieved from http://github.com/jax-ml/jax

Brown, M. C., Hervé, G., Korte, M., & Genevey, A. (2021). Global archaeomagnetic data: The state of the art and future challenges. *Physics of the Earth and Planetary Interiors*, *318*, 106766. https://doi.org/10.1016/j.pepi.2021.106766

Ertepinar, P., Hammond, M., Hill, M., Biggin, A., Langereis, C., Herries, A., et al. (2020). Extreme geomagnetic field variability indicated by Eastern Mediterranean full-vector archaeomagnetic records. *Earth and Planetary Science Letters*, *531*, 115979. https://doi.org/10.1016/j.epsl.2019.115979

Goguitchaichvili, A., Greco, C., Ruiz, R. G., Domingorena, L. P., Cejudo, R., Morales, J., et al. (2019). First archaeointensity reference palesecular variation curve for South America and its implications for geomagnetism and archaeology. *Quaternary Research*, *92*(1), 81–97. https://doi.org/10.1017/qua.2018.119

Haslett, J., & Parnell, A. C. (2008). A simple monotone process with application to radiocarbon-dated depth chronologies. *Journal of the Royal Statistical Society: Series C (Applied Statistics)*, *57*(4), 399–418. https://doi.org/10.1111/j.1467-9876.2008.00623.x

Heaton, T. J., Köhler, P., Butzin, M., Bard, E., Reimer, R. W., Austin, W. E. N., et al. (2020). Marine20 - The marine radiocarbon Age calibration curve (0-55,000 cal BP). *Radiocarbon*, *62*(4). https://doi.org/10.1017/RDC.2020.68

Hellio, G., & Gillet, N. (2018). Time-correlation-based regression of the geomagnetic field from archeological and sediment records. *Geophysical Journal International*, *214*(3), 1585–1607. https://doi.org/10.1093/gji/ggy214

Hellio, G., Gillet, N., Bouligand, C., & Jault, D. (2014). Stochastic modelling of regional archaeomagnetic series. *Geophysical Journal International*, *199*(2), 931–943. https://doi.org/10.1093/gji/ggu303

Hoffman, M. D., & Gelman, A. (2014). The No-U-Turn sampler: Adaptively setting path lengths in hamiltonian Monte Carlo. *Journal of Machine Learning Research*, *15*(47), 1593–1623. Retrieved from http://jmlr.org/papers/v15/hoffman14a.html

Hogg, A. G., Heaton, T. J., Hua, Q., Palmer, J. G., Turney, C. S., Southon, J., et al. (2020). SHCal20 Southern Hemisphere Calibration, 0-55,000 Years cal BP. *Radiocarbon*, *62*(4), 759–778. https://doi.org/10.1017/RDC.2020.59

Kanagawa, M., Hennig, P., Sejdinovic, D., & Sriperumbudur, B. K. (2018). Gaussian processes and kernel methods: A review on connections and equivalences. https://doi.org/10.48550/arXiv.1807.02582

Lanos, P. (2004). Bayesian inference of calibration curves: Application to archaeomagnetism. In *Tools for constructing chronologies: Crossing disciplinary boundaries* (pp. 43–82). Springer. https://doi.org/10.1007/978-1-4471-0231-1_3

Lanos, P., Le Goff, M., Kovacheva, M., & Schnepp, E. (2005). Hierarchical modelling of archaeomagnetic data and curve estimation by moving average technique. *Geophysical Journal International*, *160*(2), 440–476. https://doi.org/10.1111/j.1365-246X.2005.02490.x

Livermore, P. W., Fournier, A., Gallet, Y., & Bodin, T. (2018). Transdimensional inference of archeomagnetic intensity change. *Geophysical Journal International*, *215*(3), 2008–2034. https://doi.org/10.1093/gji/ggy383

Mahgoub, A. N., Juárez-Arriaga, E., Böhnel, H., Siebe, C., & Pavón-Carrasco, F. J. (2019). Late-Quaternary secular variation data from Mexican volcanoes. *Earth and Planetary Science Letters*, *519*, 28–39. https://doi.org/10.1093/gji/ggu303

McHutchon, A., & Rasmussen, C. E. (2011). Gaussian process training with input noise. In J. Shawe-Taylor, R. S. Zemel, P. L. Bartlett, F. Pereira, & K. Q. Weinberger (Eds.), *Advances in neural information processing systems* (Vol. 24, pp. 1341–1349). Curran Associates, Inc.

McIntosh, G., & Catanzariti, G. (2006). An introduction to archaeomagnetic dating. *Geochronometria: Journal on Methods & Applications of Absolute Chronology*, *25*.

Merrill, R. T., McElhinny, M. W., & McFadden, P. L. (1996). *The magnetic field of the Earth: Paleo-magnetism, the core, and the deep mantle*. Academic Press.

Molina-Cardín, A., Campuzano, S., Osete, M. L., Rivero-Montero, M., Pavón-Carrasco, F., & Palencia-Ortas, A. (2018). Updated Iberian archeomagnetic catalogue: New full vector paleosecular variation curve for the last three millennia. Geochemistry. *Geophysics, Geosystems*, *19*(10), 3637–3656. https://doi.org/10.1029/2018GC007781

Nilsson, A., Suttie, N., Stoner, J. S., & Muscheler, R. (2022). Recurrent ancient geomagnetic field anomalies shed light on future evolution of the South Atlantic Anomaly. *Proceedings of the National Academy of Sciences*, *119*(24), e2200749119. https://doi.org/10.1073/pnas.2200749119

Pavón-Carrasco, F. J., Rodríguez-González, J., Osete, M. L., & Torta, J. M. (2011). A Matlab tool for archaeomagnetic dating. *Journal of Archaeological Science*, *38*(2), 408–419. https://doi.org/10.1016/j.jas.2010.09.021

Rasmussen, C., & Williams, C. (2006). *Gaussian processes for machine learning*. MIT Press.

Reimer, P. J., Austin, W. E. N., Bard, E., Bayliss, A., Blackwell, P. G., Bronk Ramsey, C., et al. (2020). The IntCal20 Northern hemisphere radiocarbon Age calibration curve (0–55 cal kBP). *Radiocarbon*, *62*(4), 725–757. https://doi.org/10.1017/RDC.2020.41

Schanner, M. A. (2025). arthus701/pypsv: V1.2.0 [Software]. *Zenodo*. https://doi.org/10.5281/zenodo.17952306

Schanner, M. A., Korte, M., & Holschneider, M. (2022). ArchKalmag14k: A kalman-filter based global geomagnetic model for the holocene. *Journal of Geophysical Research: Solid Earth*, *127*(2), e2021JB023166. https://doi.org/10.1029/2021JB023166

Schanner, M. A., Mauerberger, S., & Korte, M. (2020). Pymagglobal - Python interface for global geomagnetic field models. *GFZ Data Services*. https://doi.org/10.5880/GFZ.2.3.2020.005

Schanner, M. A., Mauerberger, S., Korte, M., & Holschneider, M. (2021). Correlation based time evolution of the archeomagnetic field. *Journal of Geophysical Research: Solid Earth*, *126*(7), e2020JB021548. https://doi.org/10.1029/2020JB021548

Schanner, M. A., Panovska, S., & Korte, M. (2025). A hierarchical Bayesian model for the global Holocene geomagnetic field. ESSOAr (ESS Open Archive). https://doi.org/10.22541/essoar.174982568.84010657/v2

Suttie, N., & Nilsson, A. (2019). Archaeomagnetic data: The propagation of an error. *Physics of the Earth and Planetary Interiors*, *289*, 73–74. https://doi.org/10.1016/j.pepi.2019.02.008

Thébault, E., & Gallet, Y. (2010). A bootstrap algorithm for deriving the archeomagnetic field intensity variation curve in the Middle East over the past 4 millennia BC. *Geophysical Research Letters*, *37*(22). https://doi.org/10.1029/2010GL044788

Vehtari, A., Gelman, A., Simpson, D., Carpenter, B., & Bürkner, P.-C. (2021). Rank-Normalization, folding, and localization: An improved R for assessing convergence of MCMC (with discussion). *Bayesian Analysis*, *16*(2), 667–718. https://doi.org/10.1214/20-BA1221

Yu, Y., Doh, S.-J., Kim, W., Park, Y.-H., Lee, H.-J., Yim, Y., et al. (2010). Archeomagnetic secular variation from Korea: Implication for the occurrence of global archeomagnetic jerks. *Earth and Planetary Science Letters*, *294*(1–2), 173–181. https://doi.org/10.1016/j.epsl.2010.03.024

21699356, 2026, 2, Downloaded from https://agupubs.onlinelibrary.wiley.com/doi/10.1029/2025JB032670, Wiley Online Library on [07/11/2026]. See the Terms and Conditions (https://onlinelibrary.wiley.com/terms-and-conditions) on Wiley Online Library for rules of use; OA articles are governed by the applicable Creative Commons License